PHYSICAL REVIEW B **88**, 205425 (2013)

Helium-surface interaction potential of Sb(111) from scattering experiments and close-coupling calculations

M. Mayrhofer-Reinhartshuber,[1,*] P. Kraus,[1] A. Tamtögl,[1] S. Miret-Artés,[2] and W. E. Ernst[1]
[1]*Institute of Experimental Physics, Graz University of Technology, Petersgasse 16, 8010 Graz, Austria*
[2]*Instituto de Física Fundamental (IFF-CSIC), Serrano 123, 28006 Madrid, Spain*
(Received 9 October 2013; published 25 November 2013)

Helium atom scattering (HAS) was used to study the antimony Sb(111) surface beyond the hard-wall model. HAS angular distributions and drift spectra show a number of selective adsorption resonance features, which correspond to five bound-state energies for He atoms trapped in the surface-averaged He-Sb(111) potential. As their best representation, a 9-3 potential with a depth of 4.4 ± 0.1 meV was determined. Furthermore, the charge density corrugation of the surface was analyzed using close-coupling calculations. By using a hybrid potential, consisting of a corrugated Morse potential (short range) and a 9-3 potential (long range), a peak-to-peak corrugation of 17% was obtained. The kinematic focusing effects that occurred were in good agreement with surface phonon dispersion curves from already published density functional perturbation theory calculations.

DOI: 10.1103/PhysRevB.88.205425 PACS number(s): 34.35.+a, 68.49.Bc, 34.50.−s, 68.43.Mn

I. INTRODUCTION

The semimetal surfaces of antimony have recently attracted great interest since antimony is one of the basic building blocks for a number of compounds belonging to the class of topological insulators.[1,2] Moreover, Sb(111) nanofilms have proven to be an ideal test bed for the experimental investigation of topoelectronic phase transitions.[3] The film thickness and bonding to the substrate can be used to tune the electronic and spintronic properties of thin Sb films.[4,5] Hence Sb(111) films do offer attractive features for potential applications in spintronics such as a tunable band gap and spin polarization.[6]

The electronic surface states of antimony have been studied both experimentally and theoretically,[7–13] whereas for the surface dynamics of Sb(111), only theoretical investigations are available.[13] Furthermore, the atom-surface interaction as observed in scattering experiments has not been addressed, with the exception of a study of the adsorption of water on Sb(111).[14] A detailed study of the He-Sb(111) atom-surface interaction is particularly interesting not only from a fundamental point of view but also as a necessary ingredient for surface phonon measurements.

In order to understand the atom-surface interaction at semimetal surfaces helium atom scattering (HAS) is ideally suited. Experimental information about the detailed shape of the physical adsorption is most easily gained by analyzing elastic HAS intensities.[15] While semimetal surfaces are normally conducting[7,9,16] and therefore possess free surface electrons, in HAS experiments they are found to be strongly corrugated,[17,18] unlike the low-index surfaces of ordinary metals, which are perfectly flat. This may be caused by the concentration of surface electrons and holes at the Fermi energy into comparatively narrow pockets.[7,9,16] Hence semimetals are particularly interesting for HAS studies since corrugation is necessary for the occurrence of inelastic bound-state resonances which can enhance certain phonon events.[19,20] It was recently shown that inelastic HAS is capable of detecting subsurface phonon modes which are localized in layers beneath the surface in the case of metal and semimetal surfaces.[19–21] The depth to which these phonons are observable is determined by the range of the electron-phonon (e-ph) interaction, and inelastic HAS intensities can be used to infer the corresponding e-ph coupling strength.[21,22]

In a detailed analysis of the intensities on the Bi(111) semimetal surface, a mechanism for the enhancement of inelastic HAS intensities from subsurface optical modes was singled out.[23] This mechanism, which is called the surfing condition,[24] is specific to semimetal surfaces and gives rise to a strong resonance enhancement of the scattered intensities under certain kinematic conditions.[23] It involves the selective adsorption of the incident He atom into a surface-bound state due to the atom-surface interaction potential. In the case of the "surfing" situation the impinging He atom enters the bound state inelastically by creating a phonon and the trapped atom then travels at the same speed as the group velocity of the phonon along the surface. This unusual form of an atomic polaron gives rise to a strong coupling with otherwise weak subsurface phonons.[23]

Semimetal surfaces also hold the possibility of detecting electron-hole excitations via HAS due to the fact that electrons on these surfaces are restricted to narrow pockets in the parallel momentum space.[19,20] Furthermore, e-ph scattering processes at the Fermi level are likely to cause Kohn anomalies in the surface phonon dispersion,[19,20,25] an effect which has been observed with HAS for the topological insulator surfaces Bi_2Se_3 and Bi_2Te_3.[26–28]

In the present work the elastic diffraction peaks of He scattered from Sb(111) are analyzed using the exact close-coupling (CC) method.[15] This method goes beyond the simple hard-wall approximation and has been mainly applied to ionic and metallic surfaces.[29] In doing so a surface corrugation function of the system He-Sb(111) is obtained. A series of modulations of the elastic intensities due to the so-called selective adsorption resonances (SARs) is used to determine the bound-state energies of the system He-Sb(111). These energies, usually extracted from drift spectra, allow a reliable prediction of the elastic resonance conditions and are used to fit an atom-surface interaction potential. Furthermore, an enhancement of the inelastic background due to the kinematic focusing (KF) effect[24] has also been observed. The obtained atom-surface interaction potential not only is a prerequisite for surface phonon measurements but also can be exploited to enhance certain phonon events which would otherwise be too weak.

II. THEORY

In this section the minimum theoretical background necessary for the successive analysis of our measurements is presented. Throughout this work, square wave vector quantities are given in energy units, with $\hbar^2/2m = 1$, where m is the mass of the incident particles (He atoms). Furthermore, the standard notation in this field is used; that is, vectors parallel to the surface are written as boldface capital letters, and three-dimensional vectors as boldface lowercase letters.

A. The atom-surface interaction potential

In the presented experiments He atoms with a well-defined kinetic energy impinge on the sample surface. Forces originating from the interaction with each individual surface particle act on the approaching He atoms. The London dispersion (van der Waals) force, appearing because of instantaneously induced dipoles, accelerates the He atom towards the surface. The interaction between electrons of the surface and the shell of the He atom acts as a short-range counterpart, the Pauli repulsion. In contrast to electron or neutron scattering, He atoms are repelled already by the electron density a few angstroms above the topmost atomic layer.

1. 9-3 potential

Considering the contribution of these forces, the interaction between a He atom and a surface particle can be described by a 12-6 (Lennard-Jones) potential. Since one He atom is interacting with all atoms of the surface, these Lennard-Jones potentials must be summed. In the continuum limit the sums are replaced with integrals along the three space coordinates. The resulting integration over the whole semiinfinite lattice provides a 9-3 atom-surface potential given by[23]

$$V(z) = \frac{\sqrt{27}}{2} D\left[\left(\frac{\sigma}{z}\right)^9 - \left(\frac{\sigma}{z}\right)^3\right], \tag{1}$$

with z the normal distance from the surface, D the well depth of the attractive part, and σ the distance at which the potential is 0.

Using the distorted-wave Born approximation[30] the eigenvalues E_n (energy of the nth bound state) for this potential are given by

$$E_n \simeq -D\left[1 - \frac{\pi\hbar}{3.07}\frac{n+\frac{1}{2}}{\sigma\sqrt{2mD}}\right]^6. \tag{2}$$

As recently shown by Kraus *et al.*,[23] this description of the bound states is suitable for semimetal surfaces, such as Bi(111). Therefore, it is also applied for the analysis of bound states at the Sb(111) surface from HAS measurements of SARs.

2. Corrugated Morse potential (CMP)

For the analysis of the electronic corrugation, represented by the corrugation function $\xi(\mathbf{R})$, the CMP[31] is very often used in the CC framework. It can be written as

$$V(\mathbf{R},z) = D\left[\frac{1}{\upsilon_0}e^{-2\chi(z-\xi(\mathbf{R}))} - 2e^{-\chi z}\right], \tag{3}$$

with $\mathbf{r} = (\mathbf{R},z)$. χ is the stiffness parameter, and υ_0 the surface average over $e^{2\chi\xi(\mathbf{R})}$ [Eq. (6)] for the reciprocal lattice vector $\mathbf{G} = 0$]. Since $\xi(\mathbf{R})$ is periodic, Eq. (3) can be expanded in a Fourier series with

$$V(\mathbf{R},z) = V_0(z) + \sum_{\mathbf{G}\neq 0} V_{\mathbf{G}}(z)e^{i\mathbf{G}\cdot\mathbf{R}}, \tag{4}$$

where $V_0(z)$ is the bare potential and the Fourier coefficients are denoted $V_{\mathbf{G}}$. They can be expressed analytically through the corrugation Fourier coefficients $\upsilon_{\mathbf{G}}$:

$$V_{\mathbf{G}} = D\frac{\upsilon_{\mathbf{G}}}{\upsilon_0}e^{-2\chi z}. \tag{5}$$

$\mathbf{G} \neq 0$ components of Eq. (5) are also called the coupling terms of the CMP. The coefficients $\upsilon_{\mathbf{G}}$ are given by

$$\upsilon_{\mathbf{G}} = \frac{1}{\Sigma}\int_{\Sigma} e^{-i\mathbf{G}\cdot\mathbf{R}}e^{2\chi\xi(\mathbf{R})}d\mathbf{R}, \tag{6}$$

with Σ the area of the surface unit cell. The bare potential of the interaction can be written as

$$V_0(z) = D[e^{-2\chi z} - 2e^{-\chi z}]. \tag{7}$$

The bound states of the bare potential are described by an analytical expression,[32]

$$E_n = -D + \hbar\omega\left(n + \frac{1}{2}\right)\left[1 - \frac{\left(n+\frac{1}{2}\right)}{2\gamma}\right], \tag{8}$$

with n a positive integer, $\gamma = \frac{2D}{\hbar\omega}$, and $\omega = \sqrt{\frac{2\chi^2 D}{m}}$.

3. Hybrid Morse potential (HMP)

To include a more sensible, long-range interaction of the potential, a hybrid form was introduced,[33]

$$V_0 = \begin{cases} D[e^{-2\chi z} - 2e^{-\chi z}], & z \leqslant z_p, \\ -\frac{C_3}{(z-z_e)^3}, & z > z_p, \end{cases} \tag{9}$$

where both constants C_3 and z_e are chosen in a way that guarantees the continuity of the overall potential and its derivative at the inflection point z_p. While the bound states of the Morse potential can be described analytically, the ones for the HMP must be calculated numerically. Since the short-range part of the HMP is equal to the CMP, for CC calculations the same coupling terms, Eq. (5), can be used. The long-range part takes into account the asymptotic behavior of the more realistic 9-3 potential, Eq. (1).

B. Selective adsorption resonances

SARs are observed when an impinging He atom enters one of the bound states of the atom-surface interaction potential. After a short lifetime, typically 10^{-12} s, the atom leaves the surface.[34,35] Due to the phase shift of its wave function, the interference with other scattered atoms gives rise to a modulation of the scattered intensity. Several types of resonant scattering processes exist;[36–38] the most important for the present work are described below.

In the first type, a particle with an initial state (E_i, Θ_i) is elastically scattered into a bound state of energy $-|E_n|$. Thereafter, it leaves the surface potential elastically into a final state. Due to the phase shift obtained during this process, these atoms interfere with directly elastically scattered atoms and result in intensity modulations of the elastic peaks.[38]

In the second type, an incident He atom, which has elastically entered a bound state, is scattered inelastically into a final state. Due to the obtained phase shift relative to directly inelastically scattered particles, interference and hence features between the elastic peaks of the angular scans can also be observed. For this resonance type, interaction with a phonon is necessary. This scattering is also known as the phonon-assisted SAR process.[38–40]

By using the conservation laws for energy and parallel momentum, the condition for an elastic SAR can be obtained from[36,37]

$$\mathbf{k}_i^2 = (\mathbf{k}_i \sin\Theta_i + G_{\parallel})^2 + G_{\perp}^2 - |E_n|, \tag{10}$$

where $\mathbf{k}_i$ denotes the incident wave vector and Θ_i is the incident angle with respect to the surface normal. $G_{\parallel}$ and $G_{\perp}$ are the parallel and perpendicular components of the reciprocal lattice vector $\mathbf{G}$ of the surface with respect to the plane of incidence. Resonances that have a nonzero $G_{\perp}$ component are referred to as *out of plane*; resonances with $G_{\perp} = 0$, as *in plane*. To fulfill condition (10) in the experiment, either Θ_i or $\mathbf{k}_i$ can be varied, while the other is held constant. A geometrical representation of the resonance condition together with the reciprocal lattice of the first Sb(111) layer is depicted in Fig. 1.

C. Close-coupling calculations

In the CC formalism, helium atoms are considered to be structureless and nonpenetrating, while the surface is considered to be statically corrugated and periodic. In a purely elastic scattering scheme, an impinging particle with wave vector $\mathbf{k}_i$ is described by the time-independent Schrödinger equation,

$$\left[-\nabla^2 + V(\mathbf{r}) - \mathbf{k}_i^2\right]\Psi(\mathbf{r}) = 0. \tag{11}$$

While the potential is given by Eq. (4), the Fourier expanded wave function reads

$$\Psi(\mathbf{r}) = \sum_{\mathbf{G}} \Psi_{\mathbf{G}}(z) \cdot e^{i(\mathbf{K}_i+\mathbf{G})\cdot\mathbf{R}}. \tag{12}$$

If both expressions are substituted into Eq. (11), the following set of coupled equations for the diffracted waves is obtained:

$$\left[\frac{d^2}{dz^2} + \mathbf{k}_{\mathbf{G},z}^2 - V_0(z)\right]\Psi_{\mathbf{G}}(z) = \sum_{\mathbf{G}'\neq\mathbf{G}} V_{\mathbf{G}'-\mathbf{G}}(z)\Psi_{\mathbf{G}'}(z), \tag{13}$$

with $\mathbf{k}_{\mathbf{G},z}$, the z component of the particle wave vector after scattering, given by

$$\mathbf{k}_{\mathbf{G},z}^2 = \mathbf{k}_i^2 - (\mathbf{K}_i + \mathbf{G})^2. \tag{14}$$

Each of Eqs. (13) includes a characteristic effective potential $V_0 + (\mathbf{K}_i + \mathbf{G})^2$, where the second term is the asymptotic energy, which is dependent on $\mathbf{G}$ and the incident scattering conditions. All of these effective potentials have a continuous as well as a discrete spectrum. The wave functions associated with the continuum are usually expressed as $|\mathbf{K}_i + \mathbf{G}, \mathbf{k}_{\mathbf{G},z}^2\rangle$. $|\mathbf{K}_i + \mathbf{G}, n\rangle$ denotes discrete wave functions, with n the number for the nth bound state of the He-surface interaction potential. In this study the term *channel* is used for each effective potential and is usually denoted by the corresponding $\mathbf{G}[=(h,k)]$ vector: the (h,k) *channel*. Since in a fixed-angle apparatus the angle of incidence, and thus also $\mathbf{K}_i$, must be changed to measure a full angular spectrum, the asymptotic energies of the respective channels move. This phenomenon is usually called *moving thresholds*.[15,41] Two elementary kinds of scattering channels can be distinguished. For $\mathbf{k}_{\mathbf{G},z}^2 > 0$, the channels are called *open*; they are energetically accessible. In the case of $\mathbf{k}_{\mathbf{G},z}^2 < 0$, the channels are called *closed*; they are energetically forbidden channels. Though they do not produce observable features directly, a number of closed diffraction channels must be included in the simulations to achieve numerical convergence for the outcome. The higher the expected surface corrugation, the stronger are the Fourier components of the interaction potential $V_{\mathbf{G}-\mathbf{G}'}(z)$ and the more channels must be included in the calculations.[15] Nevertheless, the number of channels N has to be restricted since the computational time scales with N^3.[42]

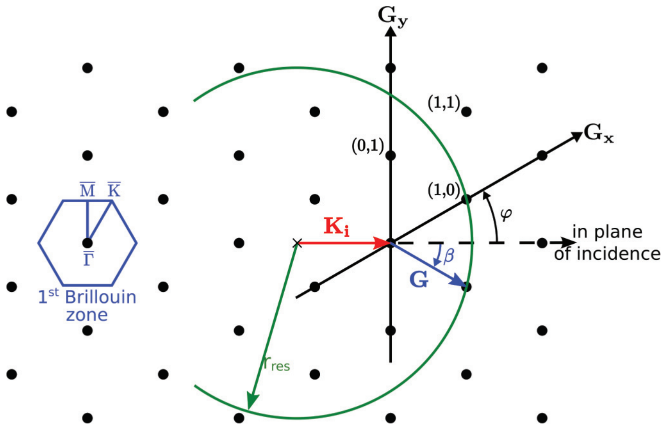

FIG. 1. (Color online) A geometrical representation of the resonance condition, Eq. (10), is shown in reciprocal space together with the first Brillouin zone for the first-layer atoms of Sb(111). The sum of the vectors $\mathbf{K}_i = \mathbf{k}_i \sin\Theta_i$ and $\mathbf{G}$, which leads to a resonant transition, lies on a circle with the radius $r_{\text{res}}^2 = \mathbf{k}_i^2 + |E_n|$.

III. EXPERIMENTAL DETAILS

A. Sb(111) surface structure

Bulk antimony exhibits a rhombohedral crystal structure (space group $R\bar{3}m$). An important feature of this structure is the puckered bilayers of atoms perpendicular to the $\langle 111\rangle$ direction. In contrast to the strong covalent bonding within these bilayers, the interbilayer bonds are of van der Waals character. Thus, the (111) surface of Sb is its natural cleavage plane,[43,44] which results in easily available Sb(111) crystal samples. The topmost layer has a hexagonal structure with an atomic spacing of $a = (4.3084 \pm 0.0002)$ Å.[45] Including second-layer atoms, the sixfold symmetry of the first layer is broken to a threefold symmetry. Nevertheless, in the HAS measurements in this study, the energy of the incident helium atoms was low enough to neglect influences of other-than-first-layer atoms.[19]

Thorough investigations of the electronic properties of Sb(111) revealed metallic surface states of the otherwise semimetallic properties of the bulk.[7–9] At the $\overline{\Gamma}$ point a hexagonal-like cut through the Fermi surface was observed. Anisotropies of the Fermi surfaces due to an anisotropy of the spin-orbit interaction led to a threefold symmetry of the intensity of six lobes surrounding this central pocket. Furthermore, at the $\overline{M}$ points oval-shaped electron pockets were detected.[7,8] Although a flat surface electron density was expected due to the Fermi surface electronic states found in all directions, with HAS measurements a surprisingly high peak-to-peak corrugation of the electron density was recently observed.[17]

B. Experimental setup

The measurements presented in this work were carried out on a HAS apparatus (H.Å.N.S.) with a fixed source-target-detector geometry $\Theta_{\rm SD} = 91.5^\circ$. By varying the temperature of the nozzle which was used for the creation of the He beam, the energy of the He atoms could be tuned between 11 and 35 meV. More details about the apparatus and its dimensions are given in a previous paper.[46] The Sb(111) single crystal used in the study was a disk with a diameter of approximately 15 mm which was cleaned by Ar^+ sputtering and annealing to 475 K prior to the measurements. The cleanliness and surface order were checked by Auger electron spectroscopy and low-energy electron diffraction, respectively.[17] All HAS measurements were performed with the crystal at room temperature (300 K). For angular scans the incident angle Θ_i of the monoenergetic He beam with respect to the surface normal was altered by rotating the sample. The angular resolution in these measurements was 0.1°. Drift spectrum measurements were obtained by varying the incident energy of the He atoms while the incident angle was held constant.

IV. RESULTS

A. He-Sb(111) potential

Angular HAS scans were performed and the observed resonance features were used to extract bound-state energies. Figure 2(a) displays the data resulting from a measurement along the $\overline{\Gamma K}$ direction. The increased intensity (solid line) of the measured He signal is plotted versus the incident angle of the He beam. The dashed curves depict the resonance conditions given by our experimental geometry, the experimental parameter $\mathbf{k}_i$, and for a given $\mathbf{G}$ vector. If this line intersects the energy of a bound state, the condition, Eq. (10), for SARs is fulfilled and maxima or minima may be observable in the measured signal. These features between the angular positions of the Bragg peaks originate from phonon-assisted SAR.

To determine the He-Sb(111) interaction potential, in the first step the bound-state energies have to be estimated. For that purpose, these energies (solid horizontal lines in Fig. 2) were varied until the angular positions of their intersections with the resonance conditions were in good agreement with the features in the measured signal. In the measurement along $\overline{\Gamma K}$ the distinct peak at $\Theta_i = 36^\circ$ and the modulations around $\Theta_i = 30^\circ$ were assigned to the in-plane resonance with the $\mathbf{G}$ vector (1,1) [(1,1) channel], whereas the high peak at $\Theta_i = 50.5^\circ$ and the small enhancements around $\Theta_i = 59^\circ$ were associated with the out-of-plane (1,0) channel. This procedure resulted in five bound-state energies, $E_{i=0\ldots4}$, which are listed in Table I.

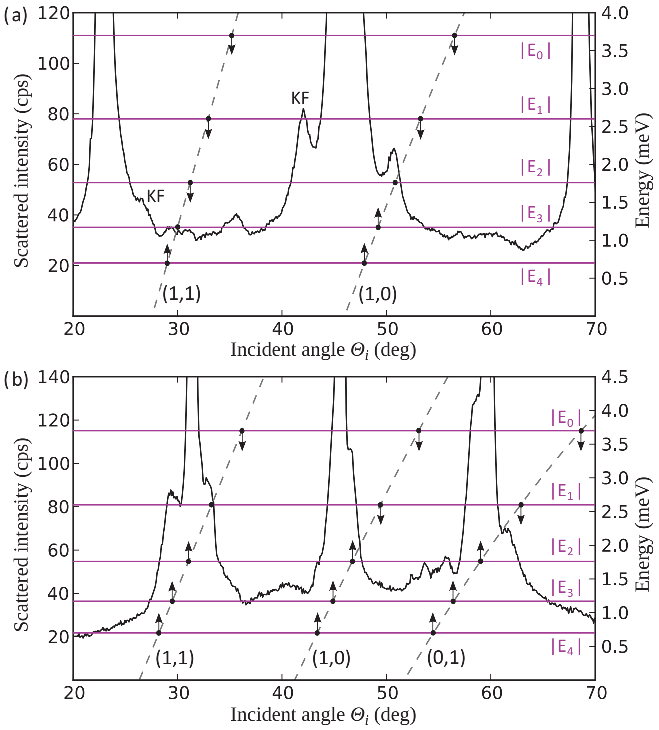

FIG. 2. (Color online) (a) Angular distribution of the HAS intensity (left-hand ordinate scale) from Sb(111) along the $\overline{\Gamma K}$ surface direction at a beam energy of 15 meV. In addition to the specular peak (45.75°) and the two closest Bragg peaks, further features corresponding to selective adsorption processes are identifiable. The five bound-state energies that were found with our measurements are depicted as horizontal lines (right-hand ordinate scale). The two dashed lines correspond to the resonance conditions for two $\mathbf{G}$ vectors [(1,0), (1,1)] in our experimental geometry and are labeled accordingly. Two additional peaks are attributed to kinematic focusing (KF) effects, which are discussed in Sec. IV D. (b) Same as (a), for an angular scan along the $\overline{\Gamma M}$ direction with resonance conditions for three $\mathbf{G}$ vectors [(1,0), (0,1), (1,1)].

The angular scan along $\overline{\Gamma M}$ is shown in Fig. 2(b). Also in this direction several features from SAR effects appear, which were included in the fitting procedure described above. The peaks at $\Theta_i = 30^\circ$ and $\Theta_i = 32^\circ$ were associated with the (1,1) channel. The shoulders of the specular (0,0) peak arise from resonances with the (1,0) channel; the shoulders of the (1,0) peak, from the (0,1) channel. Around $\Theta_i = 55^\circ$ narrow oscillations appear, which may be produced by either the (1,0) or the (0,1) channel.

It is remarkable that features originating from resonance effects with E_0 seem to result in quite small, broad intensity enhancements in the angular scans, in contrast to features with

TABLE I. Bound-state energies experimentally determined from HAS measurements and analytically calculated for the fitted 9-3 He-Sb(111) interaction potential with $D = (4.41 \pm 0.09)$ meV and $\sigma = (6.3 \pm 0.3)$ Å.

Bound state	Energy (meV) Experiment	9-3 potential, (2)
E_0	-3.7 ± 0.2	-3.7 ± 0.1
E_1	-2.6 ± 0.2	-2.6 ± 0.2
E_2	-1.86 ± 0.02	-1.8 ± 0.2
E_3	-1.17 ± 0.02	-1.2 ± 0.1
E_4	-0.70 ± 0.02	-0.8 ± 0.1

bound-state energies E_1 to E_4, which yield narrower shapes with higher intensities.

With the determined energies of the bound states, the laterally averaged He-Sb(111) interaction potential was derived. Therewith, the model potential was optimized and its analytically calculated eigenvalue spectrum was compared to the measured values with a least-squares fit. As it is a good representation of the surface, the 9-3 potential, Eq. (1), was used, whose eigenvalues are given by Eq. (2). The best fit resulted in a potential with $D = (4.41 \pm 0.09)$ meV and $\sigma = (6.3 \pm 0.3)$ Å. This well depth is in the expected range of 4–10 meV[29] and is in good agreement with values estimated in previous studies by our group.[17,47] It must be mentioned that the positions of the bound-state features are not given explicitly through this zeroth-order approximation. Nevertheless, the influence of other channels is much smaller and the bare 9-3 potential and its eigenvalues have proven to be good estimations.[23]

In Fig. 3 the obtained potential (solid black line) and its corresponding eigenvalues [dashed (blue) lines] are shown, and they agree very well with the measured values [lighter solid (red) lines]. Both experimentally and theoretically determined eigenvalues are listed in Table I, which also points out the excellent agreement. Although only 5 bound-state energies were observed in HAS measurements, the obtained potential has an eigenvalue spectrum of 14 bound states. The energies of the additional states $E_{i=5\ldots13}$ are in the region between -0.48 and -0.001 meV. Because of these closely spaced levels, a distinct assignment of features in the angular HAS scans (Fig. 2) would require a much higher resolution of the measured data. Nevertheless, in Fig. 2(b) the structures at $\Theta_i = 41^\circ$ and $\Theta_i = 53^\circ$ may arise from resonances with the bound-state energies E_5 to E_{13}.

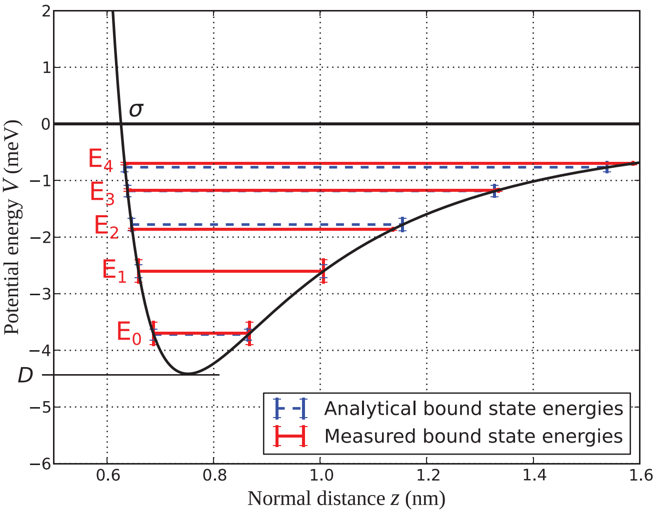

FIG. 3. (Color online) Best-fit 9-3 potential, (1), for the He-Sb(111) atom-surface interaction with $D = 4.41$ meV and $\sigma = 0.63$ nm. Lighter solid (red) lines correspond to the experimentally determined bound-state energies; dashed (blue) lines indicate the analytical bound-state values calculated with Eq. (2). Uncertainties are shown as vertical bars at the intersections with the potential.

Compared to the well depth of 8.3 meV for the He-Bi(111) interaction potential,[23] the value found for He-Sb(111) is much smaller. This is most likely caused by the higher polarizability of Bi, which causes stronger London dispersion (van der Waals) forces. In contrast to the SAR features in HAS measurements on Bi(111), the observed peaks for He-Sb(111) have both a higher absolute intensity and a much better signal-to-noise ratio. Although the measurement times were longer with HAS from Sb(111), the high intensities were far beyond expectation and should be the subject of an inelastic CC analysis.

B. Close-coupling calculations

In a previous study, the electronic surface corrugation of Sb(111) was determined from HAS by using the approximative GR method.[17] This approach is based on the hard corrugated wall (HCW) model, which neglects the actual shape and, especially, the attractive part of the atom-surface potential. For a thorough characterization of the Sb(111) surface and the He-Sb(111) interaction potential, an analysis beyond this method is required. Therefore, exact CC calculations, which are based on the determined interaction potential, were performed.

1. Kinematic analysis

For numerical convergence in terms of channels, a kinematic analysis must be carried out first. The perpendicular component of the final energy was calculated for different channels. This energy $E_{f,z}$ is a function of the incident energy E_i, the azimuthal angle, and the incident angle Θ_i. The latter is depicted in Fig. 4 for both high-symmetry directions and $E_i = 15.3$ meV. If $E_{f,z}$ is positive, the corresponding channel is open; otherwise, it is closed. It is obvious that the specular (0,0) channel (solid black line) is always open. The figure also shows channels with a (1,0) radius (green lines), a (1,1) radius (blue lines) and a (2,0) radius (red lines). To preserve the clarity of the illustration, further channels are not shown. For the sixfold geometry of the topmost Sb(111) layer, there are always six channels at a certain radius. As shown in Fig. 1, they are partly degenerated. Further degeneracies appear due to crossing of different channels. Both degeneracies are broken by the coupling coefficients of our CC calculations. Furthermore, the zero-order positions of SAR are given with the interceptions of the channels with the bound-state energies (dashed horizontal lines). The vertical lines indicate the positions of the Bragg peaks for the fixed-angle geometry of our apparatus. This particular geometry causes moving thresholds (see Sec. II C);

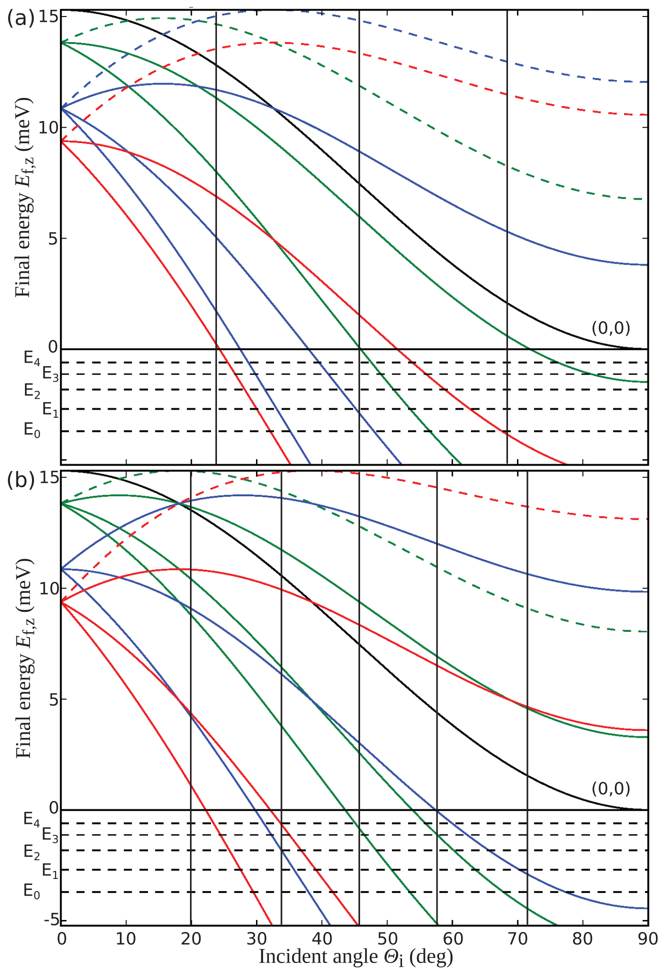

FIG. 4. (Color online) (a) Perpendicular kinetic energy $E_{f,z}$ as a function of the incident angle Θ_i with the Sb(111) crystal oriented in the $\overline{\Gamma K}$ direction and an incident energy $E_i = 15.3$ meV for He atoms. The black curve indicates the specular (0,0) channel. Green, blue, and red lines depict channels with (1,0), (1,1), and (2,0) radii, respectively. The Bragg peak positions for the experimental setup used are represented by the vertical lines. (b) Same as (a), for the $\overline{\Gamma M}$ direction.

i.e., a certain channel can cross the positions of the Bragg peaks at different energies. Usually in the CC calculations all open channels as well as closed channels with an energy close to 0 have to be included. However, for numerical convergence often more channels are taken into account, although at the cost of longer computational times.

2. *Potentials*

For further calculations, the potential V_0 and the couplings $V_{\mathbf{G}'-\mathbf{G}}$ have to be specified in the coupled equations, (13). They should represent the atom-surface interaction as precisely as possible while keeping the set of equations solvable. Usually a CMP, (3), is used for CC calculations, because the coupling terms, (5), have been derived analytically for this potential type. Since the long-range part of the HMP, (9), is similar to the more realistic 9-3 potential, the analysis of the HAS measurement was done with both the CMP and the HMP. For both types the same coupling terms, which are given by Eq. (5), were used. The parameters of these potentials were obtained in the same way as for the 9-3 potential (see Sec. IV A) and are listed in Table II. The corresponding bound-state energies are listed in Table III. As an estimation for the uncertainty, the parameter σ_E given in Table III is defined as

TABLE II. Fitted potential parameters (well depth D, stiffness parameter χ, and inflection point z_p) for the Morse as well as the hybrid (Morse/9-3) He-Sb(111) interaction potential.

Type	D (meV)	χ (Å^{-1})	z_p (Å)
CMP	4.196	0.380	–
HMP	4.252	0.395	3.0

$$\sigma_E = \frac{1}{N}\sqrt{\sum_{i=1}^{N}\left|\epsilon_i^{\text{exp}} - \epsilon_i^{\text{pot}}\right|^2}, \tag{15}$$

with N the number of bound states included. For both potentials the calculated energies of the fitted potentials are in very good agreement with the experimentally obtained values. However, the values for E_3 and E_4 are better represented by the HMP than by the CMP due to the superior asymptotic behavior.

3. *Electronic surface corrugation*

After these initial considerations, CC calculations were performed to obtain the effective electronic surface corrugation. The corrugation function $\xi(\mathbf{R})$ that we used for our model potential, (3), is given by

$$\xi(x,y) = \xi_0 \cdot \left(\cos\left[\frac{2\pi}{a}\left(x - \frac{y}{\sqrt{3}}\right)\right] + \cos\left[\frac{2\pi}{a}\left(x + \frac{y}{\sqrt{3}}\right)\right]\right) + \xi_0 \cdot \cos\left[\frac{2\pi}{a}\cdot\frac{2y}{\sqrt{3}}\right]. \tag{16}$$

It takes into account the sixfold symmetry of the topmost layer of the surface, which is the only important layer when considering the energies of the He atoms used in our experiments.[17] x and y are rectangular coordinates and ξ_0 denotes the amplitude of the corrugation to be optimized. Therewith, the amplitudes of the outgoing waves were calculated by solving the CC equations using a Numerov algorithm with a Fox-Goodwin integrator. The square moduli of these resulting amplitudes

TABLE III. Bound-state energies experimentally determined from HAS measurements and calculated analytically for the CMP and numerically for the HMP.

	Energy (meV)		
Bound state	Experiment	CMP, Eq. (8)	HMP
E_0	−3.7	−3.7	−3.7
E_1	−2.6	−2.7	−2.7
E_2	−1.86	−1.82	−1.82
E_3	−1.17	−1.13	−1.17
E_4	−0.70	−0.60	−0.72
σ_E		0.03	0.02

TABLE IV. Results of CC calculations for the CMP and HMP at different incident energies E_i. Peak-to-peak values are given for the obtained corrugation function, Eq. (16), as well as the effective corrugation function, (19), relative to the lattice constant a.

Type	E_i (meV)	ξ_{pp} (Å)	R (%)	ξ_{pp}/a (%)	$\xi_{E_i,\mathrm{pp}}/a$ (%)
CMP	15.3	0.59	6.1	13.7	9.5
CMP	21.9	0.63	7.2	14.6	9.8
HMP	15.3	0.76	4.5	17.7	12.4
HMP	21.9	0.74	3.8	17.1	11.5

are proportional to the diffraction intensities (probabilities) I_G^{calc}.[15] The geometry of our sample determines the Fourier coefficients $\upsilon_{\mathbf{G}=h\mathbf{a}^*+k\mathbf{b}^*}$ of the coupling terms, (5), to be[48]

$$\upsilon_{h,k} = \frac{\sqrt{3}}{2}\frac{a^2}{\pi}\frac{1}{2}\sum_{i=-\infty}^{\infty} I_i(\alpha)[I_{i+h}(\alpha)I_{i-k}(\alpha)+I_{i-h}(\alpha)I_{i+k}(\alpha)], \tag{17}$$

with $I_i(\alpha)$ the modified Bessel functions and $\alpha = 2\chi\xi_0$.

To account for the influence of surface vibrations at non zero surface temperatures on the intensity of the diffraction peaks, the Debye-Waller (DW) factor was included in our CC results. Its application in the analysis of HAS results has been discussed elsewhere.[17] The Debye temperature used, 155 K, was measured with HAS recently.[47]

To find the best fit between measured (P_G^{exp}) and calculated diffraction probabilities, a measure of deviation R,

$$R = \frac{1}{N}\sqrt{\sum_G \left(P_G^{\mathrm{exp}} - I_G^{\mathrm{calc}}\right)^2}, \tag{18}$$

was calculated, where N is the number of experimentally observed diffraction peaks.[29] This approach was used for both incident energies E_i, resulting in the best-fit coefficients ξ_0 listed in Table IV. The peak-to-peak corrugation ξ_{pp} was calculated for a comparison with the values obtained with the GR method in a previous analysis[17] and is also given as a percentage of the lattice constant. Especially in the case of the HMP, where the diffraction possibilities found are reproduced very well, the corrugation determined within this study is significantly higher. Since the shape of the obtained potential was included in the calculations, in particular, the results for the HMP are more accurate than the results obtained with the GR method, which uses an HCW model. Besides the fact that the CC calculations are quantum mechanically correct if convergent, they are preferable to HCW models when dealing with such high peak-to-peak corrugations as observed in this investigation.

In Fig. 5(a) the results of angular HAS scans are shown along the surface directions $\overline{\Gamma M}$ and $\overline{\Gamma K}$ at an incident beam energy of $E_i = 15.3$ meV (black line). For comparison with CC results, the areas of the experimentally measured Bragg peaks were determined (black crosses). The peak area was used instead of the intensity to account for effects such as the different widths of the Bragg peaks due to the nonzero energy width as well as the angular spread of the incident He beam. While the (red) squares in Fig. 5 indicate the best-fitting CC results that were obtained with the CMP, the

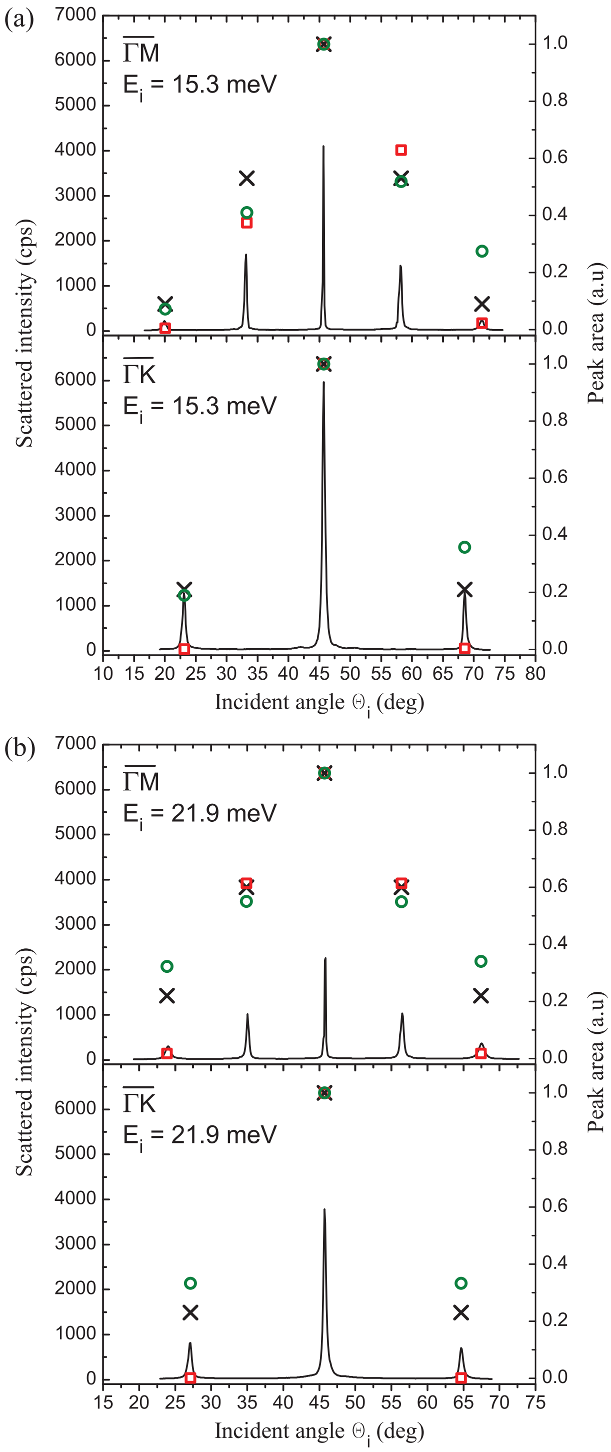

FIG. 5. (Color online) (a) Angular distributions of HAS intensity along the $\overline{\Gamma M}$ and $\overline{\Gamma K}$ surface directions at a beam energy of 15.3 meV. The peak areas (black crosses) determined from measurements (black line) are in good agreement with the best-fit results from CC calculations including the HMP [(green) circles]. Best-fit diffraction probabilities calculated with the CMP [(red) squares] show a larger deviation from the measured values. Especially when modeling the diffraction in $\overline{\Gamma K}$, the HMP is superior to the CMP. (b) Same as (a), with a beam energy of 21.9 meV. Again, the CC results for the HMP are, in contrast to the CMP, in very good agreement with the measured values.

resulting probabilities of CC calculations with the HMP are represented by (green) circles. Figure 5(b) depicts results obtained experimentally and theoretically at $E_i = 21.9$ meV. As shown in the figures and the R values in Table IV, the best fit was obtained with the HMP in CC calculations. Although there are deviations between theoretical and experimental findings, the corrugation found gives a good prediction of the measured intensities and their agreement is much better than for the CMP. Particularly, the calculations for the CMP failed to reproduce the diffraction probabilities along $\overline{\Gamma K}$ as well as the second-order probabilities along $\overline{\Gamma M}$. When the fit was adjusted to get a better agreement at these positions, the fit for the first-order diffraction peaks in $\overline{\Gamma M}$ got much worse. Hence, these values were taken for the best-fit CMP CC results. The lower intensities obtained from the measurements may be caused by the experimental setup: The measured intensities decrease with increasing angle between the specular peak and the position of measurement, which can be seen in the background signal in Fig. 2. The theoretical results in Fig. 5(a) show a remarkable asymmetry for both first- and second-order diffraction probabilities. While this is clearly noticeable in calculations with $E_i = 15.3$ meV, the results for a higher incident energy [see Fig. 5(b)] are almost symmetric. Likely, this is caused by the relative arrangement of the diffraction channels at a particular position of an elastic diffraction peak (see Fig. 4). No clear indication of such an arrangement and hence no final explanation were found, but it should be noted that small deviations between real and determined bound-state energies may have a major influence on the occurrence of such conditions during CC calculations. In order to achieve a precision of two significant digits in the results of the CC calculations, a total number of 75 channels were included.

At the position of the classical turning points of He atoms, $V(\mathbf{R},z) = E_i \cos^2 \Theta_i$ holds, which defines implicitly $[z = \xi_{E_i}(\mathbf{R})]$ the *effective corrugation function* $\xi_{E_i}(\mathbf{R})$.[49] Due to the fixed-angle geometry of the apparatus, measurements at different incident angles Θ_i are indispensable. However, for the following determination of the effective corrugation, perpendicular incidence $\Theta_i = 0^\circ$ was assumed, which yields

$$\xi_{E_i}(\mathbf{R}) = \frac{1}{\chi}\ln\left[-\frac{D}{E_i}+\sqrt{\frac{D^2}{E_i^2}+\frac{D}{E_i}\left(1+\sum_{\mathbf{G}\neq 0}\frac{v_{\mathbf{G}}}{v_0}e^{i\mathbf{G}\cdot\mathbf{R}}\right)}\right]. \tag{19}$$

Note that ξ_{E_i} depends on the incident energy E_i of the He atoms and on the well depth of the laterally averaged atom-surface interaction potential D. ξ_{E_i} is used to obtain equipotential surfaces and is usually presented as a result of CC calculations. The obtained results are listed in Table IV. Furthermore, ξ_{E_i} acts as an effective illustration of the shape of the electronic corrugation, hence it is depicted in Fig. 6.

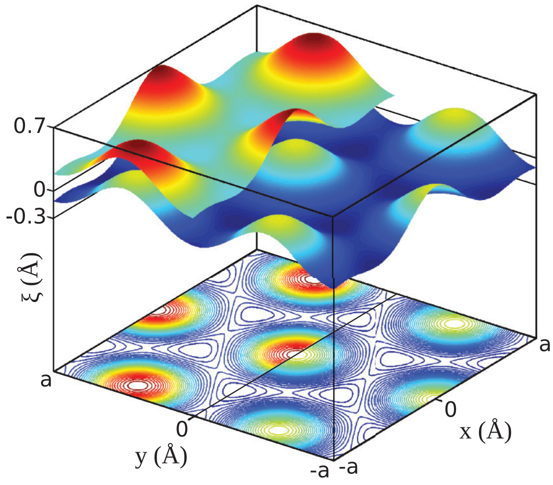

FIG. 6. (Color online) Plot of the effective corrugation for the Sb(111) surface as obtained by HAS measurements and CC calculations with the HMP for perpendicular incidence $\Theta_i = 0^\circ$. The upper part shows the result for an incident energy $E_i = 15.3$ meV, whereas the lower part shows the effective corrugation for $E_i = 21.9$ meV. In the latter case He atoms experience turning points closer to the surface.

C. Resonance effects in the specular intensity

When the intensity of the specular peak is measured as a function of the incident momentum (drift spectrum), several features of different origins appear. First, the intensity of the incident He beam depends on the nozzle temperature T_N via $1/\sqrt{T_N}$. Second, due to interference effects of waves scattered from different terraces, an oscillation of the measured signal is detectable.[29] Using the positions as well as the intensities of the major peaks and dips, the terrace height and distribution on the Sb(111) surface were estimated in a previous study.[17] Besides these main features, finer peaks and dips arise because of SAR conditions that are moving "through" the angular position of the measurement. In principle, this type of experiment is possible with an arbitrary incident angle. However, the position of the specular peak was chosen to obtain the best signal-to-noise ratio.

In Fig. 7(a) the measured specular intensity (dashed black line) is shown as a function of the energy of the incident helium beam. The nozzle temperature was varied between 53 and 150 K to achieve energies of the He atoms between 11 and 32 meV. Elastic CC calculations were used to explain the features observed in this measurement. The necessary corrugations for these calculations were obtained with a linear inter- and extrapolation of the best-fitting corrugation parameters (HMP). The obtained result [dashed black line in Fig. 7(b)] was convoluted with a Gaussian peak to take into account the energy broadening of the incident He beam [solid (red) line]. In addition, the nozzle temperature dependency of the He beam intensity and the contribution from the different terraces[17] were included and the DW attenuation was taken into account by using a surface Debye temperature of 155 K, which was determined in a previous study.[47]

In Fig. 7(a) the theoretically predicted signal is shown as the solid (green) line. It is in good agreement with the experimental data, although there is a shift of the peak near $E_i = 12$ meV. Most of the features found in the measurement could be assigned to peaks in the theoretically predicted signal, which proves the quality of the model used (the electronic surface corrugation found).

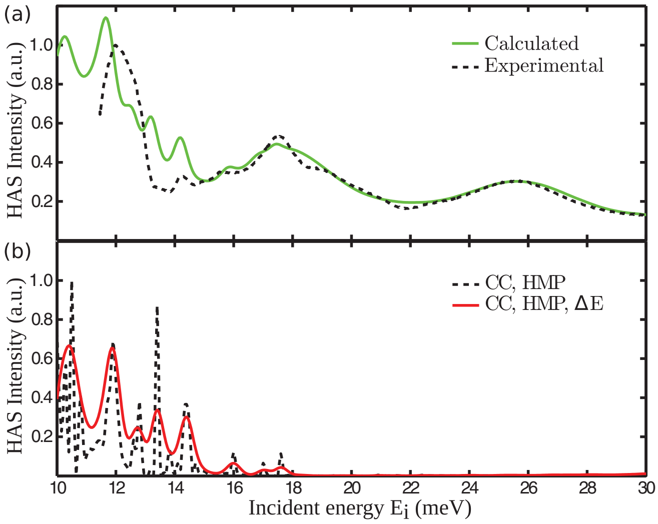

FIG. 7. (Color online) (a) Drift spectrum of the specular (0,0) peak with the sample oriented in the $\overline{\Gamma M}$ direction. The measured intensity (dashed black line) is plotted versus the incident energy E_i of the He beam. The simulated intensity [solid (green) line] is in good agreement with the experiment. (b) Results from CC calculations (dashed black line) were convoluted with a Gaussian peak to account for the energy spread ΔE of the He beam. The signal obtained [solid (red) line] was used as the SAR contribution for the calculated intensity in (a).

D. Kinematic focusing

The angular scan along $\overline{\Gamma K}$ [Fig. 2(a)] shows two additional features, at $\Theta_i = 26.5^\circ$ and $\Theta_i = 42.0^\circ$, which can be explained by the occurrence of KF.[50,51] At an angular position, where the scan curve of the HAS experiment is tangent to the surface phonon dispersion curve, an enhancement of the detected He intensity is observable. For the experimental setup used, a certain scan curve is given by[19,50]

$$\frac{\Delta E}{E_i} = \frac{\sin^2 \Theta_i}{\sin^2(\Theta_{\mathrm{SD}} - \Theta_i)} \left(1 + \frac{\Delta K}{K_i}\right)^2 - 1, \qquad (20)$$

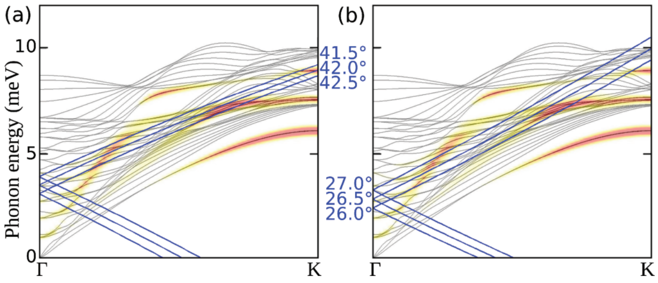

FIG. 8. (Color online) (a) Scan curves (solid blue lines) proving the KF origin of the additional peak at $\Theta_i = 42^\circ$ in Fig. 2(a). Gray lines show the dispersion curves for a 24-layer slab of Sb(111) calculated with DFPT as published by Campi *et al.*[13] Surface-localized modes and resonances for longitudinal polarization are indicated by shaded regions. For an incident angle of about 42.5°, the scan curve for phonon creation is tangent to the surface mode with an energy of between 7 and 8 meV. (b) Same as (a), with scan curves for incident angles of about $\Theta_i = 26.5^\circ$, which are tangent to the same surface phonon mode.

where ΔE is the gained (lost) energy due to phonon annihilation (creation), and ΔK the corresponding wave vector of the phonon. Although the surface phonon bands have not been measured to date, Campi *et al.*[13] used density functional perturbation theory (DFPT) to model the surface dynamics of Sb(111). Figure 8 shows the results for a slab with 24 layers as a longitudinally polarized mode along the $\overline{\Gamma K}$ direction. Furthermore, selected scan curves for our measuring geometry at incident angles around the KF positions are plotted as solid blue lines (phonon creation). It is clearly shown that the scan curves in the vicinity of these angles are tangent to the surface phonon modes, which is a prerequisite for KF appearance. The peaks found prove that KF is a reliable tool for investigation of the exact position of theoretically predicted surface phonon modes.

V. CONCLUSIONS

The He-Sb(111) interaction potential was determined by a thorough analysis of elastic HAS measurements. Clearly observable SAR features between the positions of the Bragg peaks were used to estimate five bound-state energies in the attractive well (see Table I). They were best fit with the eigenvalues of a 9-3 interaction potential with a well depth of 4.4 ± 0.1 meV. Compared to HAS on Bi(111),[23] the He-Sb(111) potential is shallower, which is the result of the lower polarizability of Sb. Furthermore, the exact CC method was applied to determine the electronic surface corrugation. Therewith, the bound-state energies were used to model potentials (CMP, HMP) suitable for CC calculations. The CC results for the CMP showed deviations from the measured intensities, most likely due to the weaker long-range part of the CMP compared to the HMP. CC results for the HMP are in good agreement with the experimental data. For the best-fitting model, HMP, a peak-to-peak corrugation of approximately 17% was obtained, which is higher than the value obtained with the less accurate HCW models.[17] The effective corrugation was found to have a peak-to-peak value of approximately 12%. Furthermore, CC calculations were used to model the intensity modulation of the specular peak as a function of the incident beam energy. The theoretical findings are in very good agreement with the measurements, which is further proof of the good quality of the He-Sb(111) interaction potential obtained. Two additional peaks found in the elastic measurements were attributed to KF effects, which were used as a coarse consistency check for the DFPT calculations of the Sb(111) surface phonon modes.[13] The He-Sb(111) interaction potential and the electronic surface corrugation obtained represent a further step towards a complete understanding of the surface properties of the semimetal antimony and its role as a building block in topological insulators. The bound-state energies determined will help in the analysis of future inelastic HAS measurements. Therewith, the experimentally determined surface phonon dispersion will be obtained and a comparison with DFPT results[13] will help to improve theoretical models of the surface dynamics. Based on our results for HAS on Bi(111),[19,20,23] mode-dependent e-ph coupling strengths will be investigated, especially if resonance-enhanced subsurface phonon modes can be detected.

In this work, we have applied the exact CC method within the framework of elastic channels. However, even in the calculation of elastic intensities and elastic SARs, couplings to inelastic channels have to be taken into account. We have used a simplified approach by including inelastic effects via a global attenuation factor: the DW factor. We think that it would be desirable to include inelastic channels in the CC framework instead of using the DW factor in order to be completely consistent. Further theoretical developments towards this goal are under way and should show whether our current approximations are sufficient.

ACKNOWLEDGMENTS

The authors wish to thank D. Campi and G. Benedek for providing calculated dispersion curves for the analysis of kinematic focusing effects. This research was supported by the European Commission and the Styrian Government within the ERDF program. S.M.A. acknowledges support from MICINN (Spain) through Grant No. FIS2011-29596-C02-01.

---

[*] Corresponding author: mayrhofer-reinhartshuber@tugraz.at

[1] H. Zhang, C.-X. Liu, X.-L. Qi, X. Dai, Z. Fang, and S.-C. Zhang, Nature Phys. **5**, 438 (2009).

[2] D. Hsieh, Y. Xia, L. Wray, D. Qian, A. Pal, J. H. Dil, J. Osterwalder, F. Meier, G. Bihlmayer, C. L. Kane, Y. S. Hor, R. J. Cava, and M. Z. Hasan, Science **323**, 919 (2009).

[3] P. F. Zhang, Z. Liu, W. Duan, F. Liu, and J. Wu, Phys. Rev. B **85**, 201410 (2012).

[4] G. Bian, T. Miller, and T.-C. Chiang, Phys. Rev. Lett. **107**, 036802 (2011).

[5] G. Bian, X. Wang, Y. Liu, T. Miller, and T.-C. Chiang, Phys. Rev. Lett. **108**, 176401 (2012).

[6] F.-C. Chuang, C.-H. Hsu, C.-Y. Chen, Z.-Q. Huang, V. Ozolins, H. Lin, and A. Bansil, Appl. Phys. Lett. **102**, 022424 (2013).

[7] K. Sugawara, T. Sato, S. Souma, T. Takahashi, M. Arai, and T. Sasaki, Phys. Rev. Lett. **96**, 046411 (2006).

[8] K. Sugawara, T. Sato, S. Souma, T. Takahashi, M. Arai, and T. Sasaki, J. Magn. Magn. Mater. **310**, 2177 (2007).

[9] H. Höchst and C. R. Ast, J. Electron Spectrosc. Relat. Phenom. **137–140**, 441 (2004) .

[10] T. Kadono, K. Miyamoto, R. Nishimura, K. Kanomaru, S. Qiao, K. Shimada, H. Namatame, A. Kimura, and M. Taniguchi, Appl. Phys. Lett. **93**, 252107 (2008).

[11] J. Seo, P. Roushan, H. Beidenkopf, Y. S. Hor, and R. J. C. A. Yazdani, Nature **466**, 343 (2010).

[12] A. Narayan, I. Rungger, and S. Sanvito, Phys. Rev. B **86**, 201402 (2012).

[13] D. Campi, M. Bernasconi, and G. Benedek, Phys. Rev. B **86**, 075446 (2012).

[14] J. Shan, A. Chakradhar, Z. Yu, and U. Burghaus, Chem. Phys. Lett. **517**, 46 (2011).

[15] A. Sanz and S. Miret-Artés, Phys. Rep. **451**, 37 (2007).

[16] P. Hofmann, Prog. Surf. Sci. **81**, 191 (2006).

[17] M. Mayrhofer-Reinhartshuber, A. Tamtögl, P. Kraus, and W. E. Ernst, J. Phys.: Condens. Matter **25**, 395002 (2013).

[18] M. Mayrhofer-Reinhartshuber, A. Tamtögl, P. Kraus, K. H. Rieder, and W. E. Ernst, J. Phys.: Condens. Matter **24**, 104008 (2012).

[19] A. Tamtögl, P. Kraus, M. Mayrhofer-Reinhartshuber, D. Campi, M. Bernasconi, G. Benedek, and W. E. Ernst, Phys. Rev. B **87**, 035410 (2013).

[20] A. Tamtögl, P. Kraus, M. Mayrhofer-Reinhartshuber, D. Campi, M. Bernasconi, G. Benedek, and W. E. Ernst, Phys. Rev. B **87**, 159906(E) (2013).

[21] I. Y. Sklyadneva, G. Benedek, E. V. Chulkov, P. M. Echenique, R. Heid, K.-P. Bohnen, and J. P. Toennies, Phys. Rev. Lett. **107**, 095502 (2011).

[22] G. Benedek, M. Bernasconi, V. Chis, E. Chulkov, P. M. Echenique, B. Hellsing, and J. P. Toennies, J. Phys.: Condens. Matter **22**, 084020 (2010).

[23] P. Kraus, A. Tamtögl, M. Mayrhofer-Reinhartshuber, G. Benedek, and W. E. Ernst, Phys. Rev. B **87**, 245433 (2013).

[24] G. Benedek, P. M. Echenique, J. P. Toennies, and F. Traeger, J. Phys.: Condens. Matter **22**, 304016 (2010).

[25] J. Kröger, Rep. Prog. Phys. **69**, 899 (2006).

[26] X. Zhu, L. Santos, R. Sankar, S. Chikara, C. Howard, F. C. Chou, C. Chamon, and M. El-Batanouny, Phys. Rev. Lett. **107**, 186102 (2011).

[27] X. Zhu, L. Santos, C. Howard, R. Sankar, F. C. Chou, C. Chamon, and M. El-Batanouny, Phys. Rev. Lett. **108**, 185501 (2012).

[28] C. Howard, M. El-Batanouny, R. Sankar, and F. C. Chou, Phys. Rev. B **88**, 035402 (2013).

[29] D. Farias and K.-H. Rieder, Rep. Prog. Phys. **61**, 1575 (1998).

[30] M. W. Cole and T. Tsong, Surf. Sci. **69**, 325 (1977).

[31] G. Armand and J. R. Manson, J. Phys. (France) **44**, 473 (1983).

[32] P. M. Morse, Phys. Rev. **34**, 57 (1929).

[33] H. Hoinkes, Rev. Mod. Phys. **52**, 933 (1980).

[34] R. B. Doak, Ph.D. thesis, Massachusetts Institute of Technology, 1981.

[35] M. I. Hernández, J. Campos-Martínez, S. Miret-Artés, and R. D. Coalson, Phys. Rev. B **49**, 8300 (1994).

[36] V. Celli, in *Helium Atom Scattering from Surfaces*, edited by E. Hulpke (Springer, Berlin, 1992), p. 25.

[37] H. Hoinkes and H. Wilsch, in *Helium Atom Scattering from Surfaces*, edited by E. Hulpke (Springer, Berlin, 1992), p. 113.

[38] S. Miret-Artés, Surf. Sci. **366**, L735 (1996).

[39] G. Brusdeylins, R. B. Doak, and J. P. Toennies, J. Chem. Phys. **75**, 1784 (1981).

[40] G. Lilienkamp and J. P. Toennies, J. Chem. Phys. **78**, 5210 (1983).

[41] M. Hernández, S. Miret-Artés, P. Villarreal, and G. Delgado-Barrio, Surf. Sci. **251–252**, 369 (1991).

[42] R. Martínez-Casado, B. Meyer, S. Miret-Artés, F. Traeger, and C. Wöll, J. Phys.: Condens. Matter **19**, 305006 (2007).

[43] B. Stegemann, C. Ritter, B. Kaiser, and K. Rademann, Phys. Rev. B **69**, 155432 (2004).

[44] S. Bengió, J. Wells, T. Kim, G. Zampieri, L. Petaccia, S. Lizzit, and P. Hofmann, Surf. Sci. **601**, 2908 (2007).

[45] D. Schiferl and C. S. Barrett, J. Appl. Crystallogr. **2**, 30 (1969).

[46] A. Tamtögl, M. Mayrhofer-Reinhartshuber, N. Balak, W. E. Ernst, and K. H. Rieder, J. Phys.: Condens. Matter **22**, 304019 (2010).

[47] A. Tamtögl, M. Mayrhofer-Reinhartshuber, P. Kraus, and W. E. Ernst, Surf. Sci. **617**, 225 (2013).

[48] P. Kraus, M. Mayrhofer-Reinhartshuber, A. Tamtögl, S. Miret-Artés, and W. E. Ernst (unpublished).

[49] S. Miret-Artes, J. P. Toennies, and G. Witte, Phys. Rev. B **54**, 5881 (1996).

[50] G. Benedek, Phys. Rev. Lett. **35**, 234 (1975).

[51] G. Benedek, G. Brusdeylins, J. P. Toennies, and R. B. Doak, Phys. Rev. B **27**, 2488 (1983).